JGR Solid Earth

RESEARCH ARTICLE
10.1029/2022JB025119

Structure and Dynamics in Liquid Iron at High Pressure and Temperature. A First Principles Study

Luis E. González[1] and **David J. González**[1]

[1]Departamento de Física Teórica, Universidad de Valladolid, Valladolid, Spain

Key Points:

- Liquid iron is studied ab initio for pressures up to 323 GPa
- Static and dynamic structural properties are considered
- Transport properties are obtained

Correspondence to:

L. E. González,
luisen@metodos.fam.cie.uva.es

Citation:

González, L. E., & González, D. J. (2023). Structure and dynamics in liquid iron at high pressure and temperature. A first principles study. *Journal of Geophysical Research: Solid Earth*, *128*, e2022JB025119. https://doi.org/10.1029/2022JB025119

Received 20 JUL 2022
Accepted 8 FEB 2023

Author Contributions:

Conceptualization: Luis E. González
Data curation: David J. González
Funding acquisition: Luis E. González
Investigation: Luis E. González, David J. González
Software: Luis E. González
Supervision: David J. González
Writing – original draft: David J. González
Writing – review & editing: Luis E. González

Abstract We have studied the evolution of structural and dynamic properties of liquid Fe as a function of pressure for 11 thermodynamic states close to the melting line. The pressure range considered goes from ambient pressure to 323 GPa, and the study has been carried out by using the ab-initio molecular dynamics technique. The agreement between the calculated static structure and the available experimental data is very good, including details like an asymmetric second peak, which remains over most of the whole pressure range and suggests a significant local icosahedral short-range order in the liquid. The dynamical structure is studied through the characteristics of the propagating density fluctuations and the associated longitudinal and transverse particle currents. The transverse dispersion relations expose two branches of modes for all pressures, whose range of appearance is analyzed and put in connection with the double-peak structure of the Fourier spectra of velocity autocorrelation functions. We have also investigated the existence of fingerprints of transverse acoustic excitation modes in the dynamic structure factor for the high pressure states similar to those observed in the inelastic X-ray scattering intensity data of liquid Fe at ambient pressure. The calculated electronic density of states shows that with increasing pressure there is a widening of the conduction band along with a decreasing significance of spin polarization. Finally, we also report results for transport coefficients like self-diffusion, shear viscosity and adiabatic sound velocity, which are compared with the available experimental data.

Plain Language Summary The Earth's core is mainly composed of iron, with an inner solid core below a depth of 5,150 km, where the pressure exceeds 3.3 million atmospheres, and an outer liquid core, between 2,900 and 5,150 km below the Earth's surface, where the pressure ranges from 1.3 to 3.3 million atmospheres, with absolute temperatures from 4000 to 6500 K. The experimental determination of the properties of liquid iron at these conditions is extremely difficult, and therefore alternative types of studies are very convenient in order to understand the behavior of the liquid outer core. In this paper we perform computer simulations to study the properties of liquid iron from ambient pressure to values typical of the boundary between the outer liquid core and the inner solid core. This is done by starting from very basic ingredients, such as the electronic structure of atomic iron. From these, Quantum Physics leads to interatomic forces, which are used in the computer simulations to generate atomic configurations typical of the liquid at several temperatures and pressures. Finally the properties of the liquid, such as its structure, viscosity, and several others, are obtained using Statistical Physics tools.

1. Introduction

Iron is the most abundant element in the Earth's core, especially in the liquid outer core (LOC), but also in the solid inner core, where other elements are present in significant concentration. Therefore Fe is very relevant in geophysics. The LOC stretches between ∼2,900 and 5,150 km depth, covers a pressure and temperature range from 135 to 330 GPa and from 4000 to 6500 K respectively, and comprises around 96% of the total core's volume. Consequently, the study of the properties of liquid iron (l-Fe) in such a high temperature and pressure regime is a topic of geophysical interest. The understanding of important phenomena that occur in the core, such as the generation of the magnetic field, and the heat and mass transport, requires a good knowledge of the dynamic properties of l-Fe.

Without intending to be exhaustive of the wealth of research already performed about l-Fe, we make below a short review of those aspects that have been studied and are related to our present work. We will mention experimental measurements and theoretical calculations, based on Molecular dynamics (MD) simulations, that have addressed thermodynamic, structural and transport properties of l-Fe.

Starting with experiments, it is fair to acknowledge the inherent practical difficulties associated to the extreme conditions. Nevertheless, some data about the thermodynamic (Anderson & Ahrens, 1994; Dobson, 2002; Dubrovinsky et al., 2000; Nasch et al., 1994; Rutter et al., 2002; Secco et al., 2002) and structural (Inui et al., 2009; Kuwayama et al., 2020; Sanloup et al., 2000; Schenk et al., 2002; Shen et al., 2004; Waseda, 1980) properties of iron have already been gathered.

The static structure factor, $S(q)$, of l-Fe near its melting point at ambient pressure was measured by X-ray diffraction (XD) (Inui et al., 2009; Waseda, 1980) and neutron diffraction (ND) (Schenk et al., 2002) techniques. Later, Shen et al. (2004) extended XD measurements of $S(q)$ to higher pressures, up to 58 GPa, while more recently Kuwayama et al. (2020) managed to reach pressures of 116 GPa. It was found that, within this range, the $S(q)$ preserves a shape qualitatively similar to that observed at ambient pressure.

The dynamic structure of l-Fe at ambient pressure and 1843 K was studied by Hosokawa et al. (2008) through inelastic X-ray scattering (IXS) experiments. In the scattered intensities for wavevectors $q \leq 2.13$ Å^{-1}, they observed clear side peaks due longitudinal acoustic excitations, while a closer analysis of the results for some q's, revealed some additional excitations appearing as weak shoulders located in a narrow frequency range between the quasielastic peak and the inelastic (longitudinal) excitation peaks. These additional excitations were considered fingerprints of transverse acoustic (TA) modes. Contrary to the static structure, no measurements of the dynamic structure have been carried out at higher pressures.

When it comes to theoretical approaches, the problems regarding thermodynamic states in the high pressure and temperature regime are much less severe. Consequently there have already been many theoretical studies that address a variety of thermodynamic, structural, electronic and transport properties of solid and liquid iron, as well as several iron-based alloys (Alfe, 2009; Alfe et al., 2000; Belonoshko et al., 2011; Fomin et al., 2013; Gillan et al., 2006; Vocadlo et al., 1997, 2003; Zeng et al., 2008). MD techniques stand up as one of the methods most widely used to perform these investigations. MD simulations can be classified into classical molecular dynamics (CMD), where interactions among atoms are obtained from effective model potentials, and ab-initio molecular dynamics (AIMD) where the energy and forces are obtained from electronic structure calculations performed along the ionic MD trajectory, taking account of the quantum mechanical nature of the electron mediated interactions, and therefore providing a higher accuracy as compared to CMD. Most AIMD methods rely on the density functional theory (DFT), (Hohenberg & Kohn, 1964; Kohn & Sham, 1965) which render such electronic structure calculations affordable, even if still very costly computationally.

CMD simulations have covered the whole pressure range, from ambient pressure up to the highest one corresponding to the LOC. Most of these simulations used the effective potential known as embedded-atom model (Sutton & Chen, 1990) to study both solid and l-Fe (Belonoshko et al., 2000; Bryk & Belonoshko, 2012; Koci et al., 2006). Specifically, the model developed by Belonoshko et al. (2000) has been widely used. For instance, to investigate the melting of the hcp phase of Fe at high pressure (Belonoshko et al., 2000), to study (Koci et al., 2006) the static structure of l-Fe at the same thermodynamic states experimentally investigated by Shen et al. (2004), to analyze several static and dynamic properties of l-Fe near the melting point at ambient pressure (Bryk & Belonoshko, 2012), or to study the variation of some transport coefficients of l-Fe along the melting line at those thermodynamics states associated with the LOC (Fomin et al., 2013).

AIMD simulations of l-Fe, however, have been mainly focused on the high pressure and temperature regime, dating back to 1997 when Vocadlo et al. (1997) obtained the structure factor of l-Fe at 4300 and 6000 K, which are roughly the limits of the temperature range in the LOC. Later AIMD studies have addressed structural properties (Alfe et al., 2000; Vocadlo et al., 2003), transport coefficients (self-diffusion and shear viscosity) (Alfe et al., 2000; de Wijs et al., 1998), adiabatic sound velocity (Alfe et al., 1999, 2002) or the melting curve (Alfe et al., 1999, 2002, 2004).

Surprisingly, the low pressure states have been far less studied by AIMD techniques. The first study was produced by Ganesh and Widom (2008) and was focused on several static properties. They found that in order to obtain a good description of the short range order in l-Fe it was necessary to include atomic magnetic moments in the calculation, thus requiring the use of the spin polarized version of DFT. Recently, we have performed an AIMD study of l-Fe at ambient and some high pressure states (Marques et al., 2015, 2016) with the main emphasis focused on the calculation of several dynamic properties because of the availability of the IXS data of Hosokawa et al. (2008). We found that not only the static structure was sensitive to the use of atomic magnetic moments,

Table 1
Thermodynamic States Studied in This Work and Number of Equilibrium Configurations Included in the Study

P (GPa)	ρ (Å^{-3})	T (K)	N_{Conf}
0	0.0751	1873	12,000
28	0.0966	2560	12,000
42	0.1015	2650	15,000
58	0.1053	2900	16,500
76	0.1090	3500	18,000
96	0.1120	3800	18,000
157	0.1220	4500	20,000
202	0.1280	5000	20,000
262	0.1350	5700	20,000
293	0.1380	6150	20,000
323	0.1390	6370	20,000

Note. ρ is the ionic number density and T is the temperature.

but that dynamic properties were even more sensitive, producing values way off the experimental ones when spin polarization was ignored. Nonetheless, it was observed that the increase in pressure turned smaller the influence of spin polarization.

In this paper we report an AIMD simulation study of several static and dynamic properties of l-Fe at diverse thermodynamic states near the melting line. We aim to explore the connection among static structure, single particle and collective dynamics. Interestingly, for some states it will be possible to compare with experiment because the associated static structure factors have been measured by XD experiments (Kuwayama et al., 2020; Shen et al., 2004).

Also, we are interested in analyzing the pressure dependence of the main dynamical collective processes, that is, sound and shear waves, as it has recently been found that with increasing pressure, the transverse dispersion relation develops a second, higher frequency branch which is not present at ambient conditions.

In the following sections we describe the method we used, together with the parameters employed and some technical details, we report on the results obtained and their comparison with previously available data, and finally we draw some conclusions of our study.

2. Computational Method

AIMD simulations have been performed for l-Fe at various thermodynamic states along its melting line with pressures ranging from ambient pressure (0 GPa) to 323 GPa and temperatures up to ≈6400 K. Those thermodynamics states, along with other technical details, are listed in Table 1 and are also plotted in Figure 1.

These AIMD simulations were carried out within DFT, using the Vienna ab initio simulation package (Kresse & Furthmuller, 1996). The electron-ion interaction was described by means of projected augmented wave all-electron potentials (Kresse & Joubert, 1999), with 14 valence electrons ($3p^6$, $3d^6$, $4s^2$) in order to take into account the semicore electrons. The electronic exchange-correlation energy was described by the Perdew-Burke-Ernzerhof generalized gradient exchange-correlation functional (Perdew et al., 1996). The electronic wave functions were represented in terms of a plane-wave basis set with an energy cutoff of 300 eV.

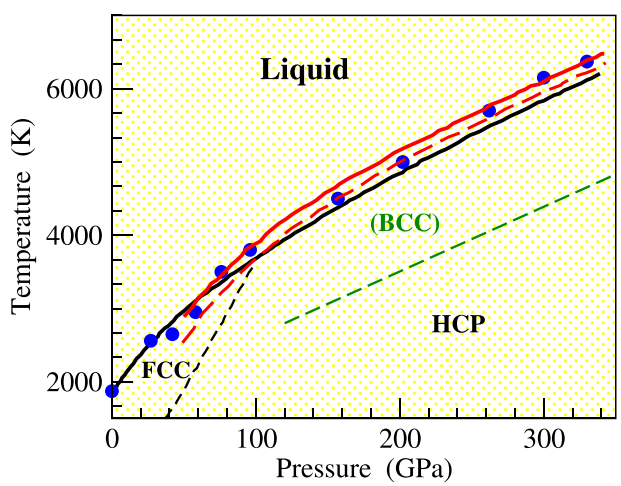

Figure 1. Pressure-temperature phase diagram of Fe. Full and broken red lines: ab-initio molecular dynamics (AIMD) simulations of Alfe et al. (1999, 2002). Full black line: laser-heated experiments of Anzellini et al. (2013). Broken green line: Boundary line between hcp and bcc phases, as suggested by Belonoshko et al. (2021). Blue circles: present AIMD simulation state points.

The simulations were performed in the microcanonical ensemble, using 100 atoms inside a cubic cell with periodic boundary conditions and whose size was the appropriate for a given ionic number density. Newton's equations of motion were integrated using Verlet's algorithm in the velocity form with a time step of 2 fs. The sampling of the Brillouin zone was performed by means of the single Γ-point. Spin polarization was included for the lower pressure states (less than 100 GPa) with the spin-interpolation of the correlation energy proposed by Vosko et al. (1980).

The initial configurations were chosen randomly and the equilibration process lasted 5 ps, and therefrom the microcanonical simulations spanned 22–40 ps, depending on the thermodynamic state. Those equilibrium configurations were subsequently employed for the evaluation of several static, dynamic and electronic properties of bulk l-Fe along the melting line.

We point out that this same AIMD simulation method was used by Alfe et al. (1999, 2002, 2004) to study the high pressure melting curve of Fe. Their calculated melting curve is very close to that experimentally determined by Anzellini et al. (2013) by using a laser-heated diamond-anvil cell. Therefore, the input data we have used in the present study (see Table 1) are those

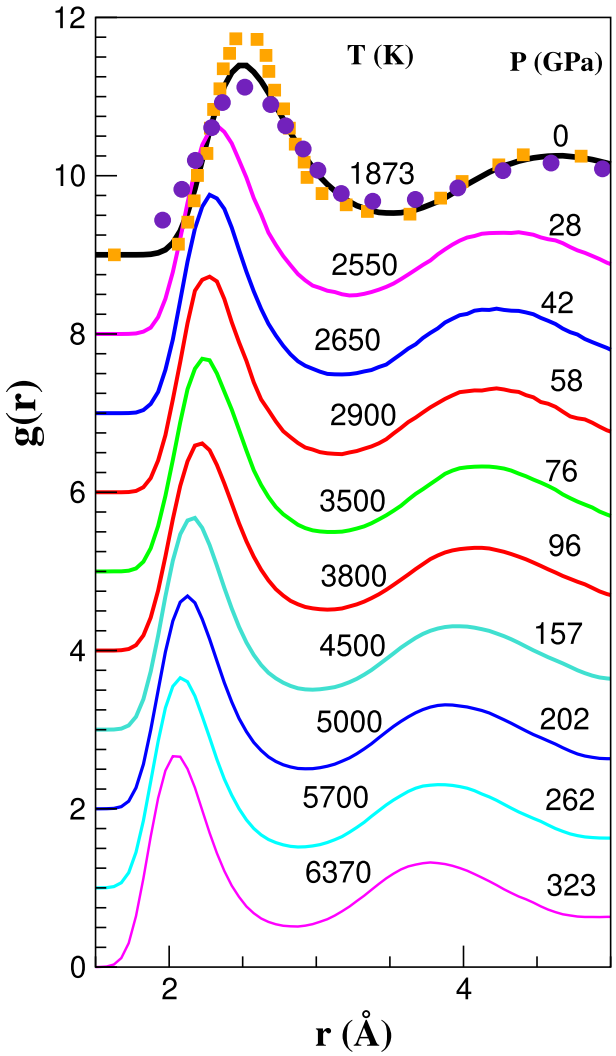

Figure 2. Pair distribution function, $g(r)$, of l-Fe at different pressures along the melting line. Continuous line: ab-initio molecular dynamics simulations. Full circles and squares: experimental neutron diffraction data (Schenk et al., 2002) and X-ray diffraction data (Inui et al., 2009) respectively, for ambient pressure.

evaluated by Alfe et al. (1999, 2002, 2004), which differ slightly from those used in our previous studies (Marques et al., 2015, 2016).

3. Results

3.1. Static Properties

The atomistic structure in liquids is usually characterized by the pair distribution function, $g(r)$, and the static structure factor, $S(q)$, with both magnitudes being directly generated in the AIMD simulations. The obtained AIMD simulation results for $g(r)$ at several pressures along the melting line are plotted in Figure 2. As expected, the position of the main peak, r_p, moves toward smaller r-values with increasing pressure; on the other hand its height, $g(r_p)$, initially increases from 2.40 at ambient pressure to 2.74 at $P = 58$ GPa, and then decreases slightly for higher pressures to a minimum value of ≈2.63 at $P = 323$ GPa.

The coordination number (CN) is a magnitude that informs about the average number of nearest neighbors (NNs). We have obtained it by integrating the radial distribution function (RDF), $G(r) = 4\pi\rho r^2 g(r)$, up to the position of its first minimum, R_{min}. The obtained values for CN are given in Table 2, where it is observed that it remains practically constant (≈12.6) over the whole pressure range. It is worth noticing that analogous studies for other liquid metals along their respective melting curves have yielded qualitatively different results. Thus, recent studies of l-Al (Jakse & Bryk, 2019) and l-Pb (Bryk et al., 2019) along their respective melting lines up to 320 and 70.5 GPa respectively, showed an increase of the CN with rising pressure. On the other hand, similar studies for l-Li and l-Rb (Bryk et al., 2013; Tamblyn et al., 2008) showed the opposite tendency of a reducing CN with increasing pressure. Such an invariant CN in the case of Fe, suggests a uniform compression with increasing pressure, so we have analyzed this possibility in greater detail.

First, we have evaluated the distribution of distances to the ith NN, through the partial RDF (McGreevy et al., 1986), $G_i(r)$ ($i = 1, 2, \cdots$). The position of its maximum is identified with the ith NN average distance, and we have analyzed its evolution with increasing pressure. If the system would compress uniformly, the average NN distances would scale according to the cubic root of the number density, so we have plotted in Figure 3 the scaled average NN distances as a function of pressure.

We observe that the scaled average interatomic distances exhibit some changes within the pressure range up to ≈100 GPa only, and therefrom there is hardly any variation. Inside the first coordination shell (which includes up to the 13th NN), we find a trend that points to two subshells with opposite behaviors. One subshell includes up to the 6th NN, and the other comprises from the 7th to the 13th NN. In the first subshell, we note that the reduced average interatomic distances increase with pressure until ≈50 GPa and then decrease until ≈100 GPa. The opposite behavior is observed for the second subshell, where the reduced distances initially decrease (up to 50 GPa) and then increase up to 100 GPa. Therefrom, when the pressure is further increased all the way up to 323 GPa, it does not affect the reduced average interatomic distances. Within the second coordination shell, we notice that the reduced average interatomic distances of the 14th and 15th NNs remain practically constant whereas those corresponding to the 16th–25th NNs show a very similar trend as that of the first subshell. We can therefore conclude that compression is not exactly uniform for pressures up to 100 GPa (it is so for higher pressures), but the radial rearrangement of the NNs is in fact very small.

Additional insight into the structural changes undergone by l-Fe upon compression is provided by the common neighbor analysis (CNA) (Honeycutt & Andersen, 1987). This method gives three dimensional information about

Table 2
Calculated Values of the Position, q_p(Å^{-1}), and Height, $S(q_p)$, of the Main Peak of S(q), Position of the Main Peak of g(r), r_p(Å), Position of the First Minimum of G(r), R_{min} (Å), and Coordination Number (CN), for the Different States

P (GPa)	q_p	$S(q_p)$	r_p	$R_{\min}$	CN
0	3.00	3.05	2.50	3.42	12.6
28	3.25	3.00	2.33	3.13	12.6
42	3.31	3.00	2.29	3.08	12.6
58	3.33	2.95	2.26	3.04	12.6
76	3.35	2.92	2.24	2.99	12.5
96	3.42	2.92	2.22	2.95	12.5
157	3.50	2.92	2.17	2.87	12.5
202	3.54	2.92	2.13	2.85	12.5
262	3.57	2.92	2.08	2.79	12.6
293	3.62	2.92	2.07	2.78	12.6
323	3.66	2.92	2.05	2.75	12.6

the local environment around each atomic pair contributing to the peaks of the $g(r)$, and this information is presented in terms of the number and properties of the common nearest neighbors of the pair under consideration. The method allows to discriminate among different local structures such as bcc, hcp, fcc and icosahedral, according to the abundance of different types of pairs. For example, 142x-type pairs are characteristic of close-packed (CP) structures, namely fcc and hcp ordering, the bcc is typified by 144x and 166x pairs whereas the 15xx (sum of 1,551 and 1,541) is related to icosahedral ordering. Finally, the 1,431 type pairs are linked to distorted icosahedral structures or distorted CP structures.

For each thermodynamic state, four AIMD configurations were chosen and the corresponding inherent structures (local minimum of the potential energy surface) were obtained; subsequent application of the CNA method, and averaging over the four configurations considered, yielded the results plotted in Figure 4. It is found that the icosahedral ordering (15xx and 1,431) is the most abundant in l-Fe, for the whole pressure range, with a starting value of ≈65% of the pairs which remains nearly constant until ≈200 GPa and therefrom it smoothly increases with pressure reaching a value of ≈72% at 323 GPa. The 142x-type pairs, which are related to CP structures, show some increase with pressure, reaching a 10% of the pairs at ≈100 GPa and remain nearly constant up to 323 GPa. The total amount of 1,441 and 1,661 type pairs, indicative of bcc ordering, starts at around 20% of the pairs and

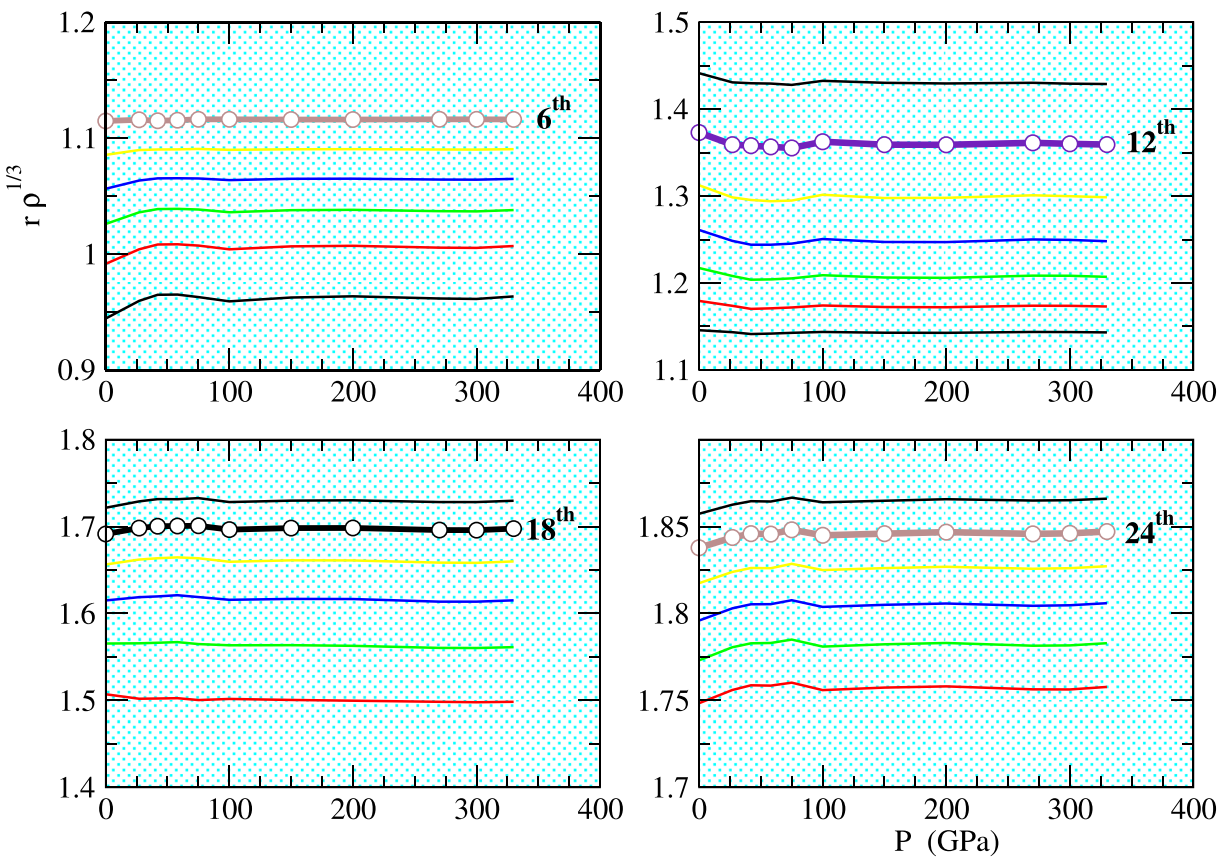

Figure 3. Pressure dependence of the reduced average interatomic distance to the 1st, 2nd ….up to the 25th nearest neighbor along the melting line in l-Fe for a range of pressures up to 323 GPa. The thick curves with open circles correspond to the 6th, 12th, 18th, and 24th nearest neighbor. For each state, the distances are normalized with respect to the cubic root of the respective ionic number density, namely $\rho^{1/3}$.

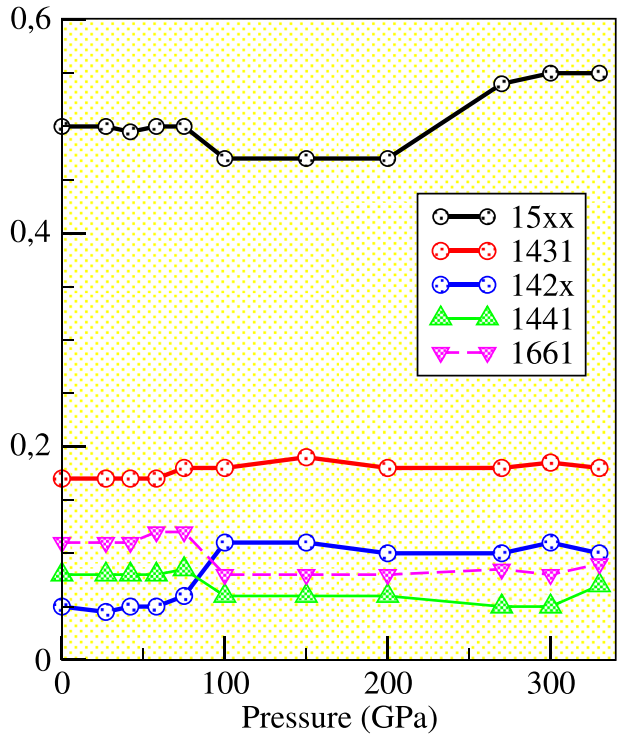

Figure 4. Pressure dependence of the most abundant bonded pairs.

shows a gradual reduction with increasing pressure reaching 15% of the pairs at ≈100 GPa, then it remains practically constant when the pressure is further increased up to 323 GPa. Notice that the fraction of bcc ordering lost with increasing pressure up to ≈100 GPa, is the same amount gained by the CP structures.

Figure 5 shows the AIMD results for the static structure factors, $S(q)$, which display a symmetric main peak whose position, q_p, smoothly increases with rising pressure (see Table 2). Moreover, the second peak shows a small shoulder located at the high-q side, whose intensity remains practically unaffected up to ≈200 GPa; then it gradually abates until it is hardly noticeable at the highest pressure. This feature has also been found in several other liquid transition metals and has been linked to the existence of a significant amount of icosahedral local order. In Figure 5 we have also depicted the available experimental XD and ND data for $S(q)$, which have been measured for ambient (Inui et al., 2009; Schenk et al., 2002) and high pressure states (Kuwayama et al., 2020; Shen et al., 2004). More specifically, Kuwayama et al. (2020) performed XD measurements of l-Fe at several high pressure states which are close, although not identical, to the states considered in the present AIMD simulation.

The long wavelength limit of the structure factor, $S(0)$, has been used to obtain an estimate for the isothermal compressibility, κ_T, of l-Fe along the melting line. First, the low q-values of $S(q)$ were quadratically extrapolated to $q \to 0$, by a least squares fitting, $S(q) = s_0 + s_2 q^2$, of the calculated values for $q \leq 1.2$ Å^{-1} and the results are reported in Table 3. Then, we have used the relation $S(0) = \rho k_B T \kappa_T$ where k_B is Boltzmann's constant, to obtain an estimate for κ_T. The result at ambient pressure ($\kappa_T \approx 1.24 \pm 0.11$) agrees well with the corresponding experimental data $\kappa_T \approx 1.21 \pm 0.02$ (Hixson et al., 1990), but for higher pressures our data must be considered as a prediction, since no experimental results are available.

3.2. Dynamic Properties

3.2.1. Single Particle Dynamics

We analyze the single particle dynamics through the normalized velocity autocorrelation (VACF), $Z(t)$, defined as

$$Z(t) = \langle \vec{v}(t + t_0) \cdot \vec{v}(t_0) \rangle / \langle \vec{v}(t_0) \cdot \vec{v}(t_0) \rangle \quad (1)$$

where the average is over particles and time origins. The calculated $Z(t)$ are depicted in Figure 6, and display the typical behavior of a dense liquid, with a rapid decay followed by a pronounced minimum and additional weak oscillations. This first minimum is related to a backscattering effect induced by the cage formed by its NNs; moreover, with increasing pressure its position moves toward shorter times which points to a stronger vibrational motion induced by the contraction of the cage. The average frequency of this vibrational motion is known as the Einstein frequency, ω_E, and can be obtained from a short time expansion of $Z(t)$, namely, $Z(t) = 1 - \omega_E^2 t^2/2 \ldots$. A fit of the AIMD $Z(t)$ to this formula for short times provides an estimation of the ω_E, whose values are given in Table 4 for the different pressures considered.

The time integral of $Z(t)$, and also the slope of the mean square displacement of any particle, $\delta R^2(t) \equiv \langle |\vec{R}_1(t) - \vec{R}_1(0)|^2 \rangle$, are related to the self-diffusion coefficient, D. The values obtained for D at the different thermodynamic states studied are shown in Table 4. First, we note that the AIMD result at ambient pressure, $D \approx 0.320$ Å^2/ps compares rather well with the semiempirical value, estimated by Iida et al. (2006) from experimental data for other thermodynamic magnitudes, of $D_{\text{exp}} \approx 0.355$ Å^2/ps. When the pressure is increased along the melting line, the calculated D decreases attaining a value of $D \approx 0.212$ Å^2/ps for $P = 58$ GPa; therefrom, when pressure is further increased the calculated D increases all the way up to $P = 323$ GPa. This nonmonotonic behavior can be understood by noting that the self-diffusivity along the melting line is the result of the interplay of two competing factors: an increase in density which causes a drop in the diffusivity and an increase in temperature which enhances the mobility of the atoms. We note that a qualitatively similar variation

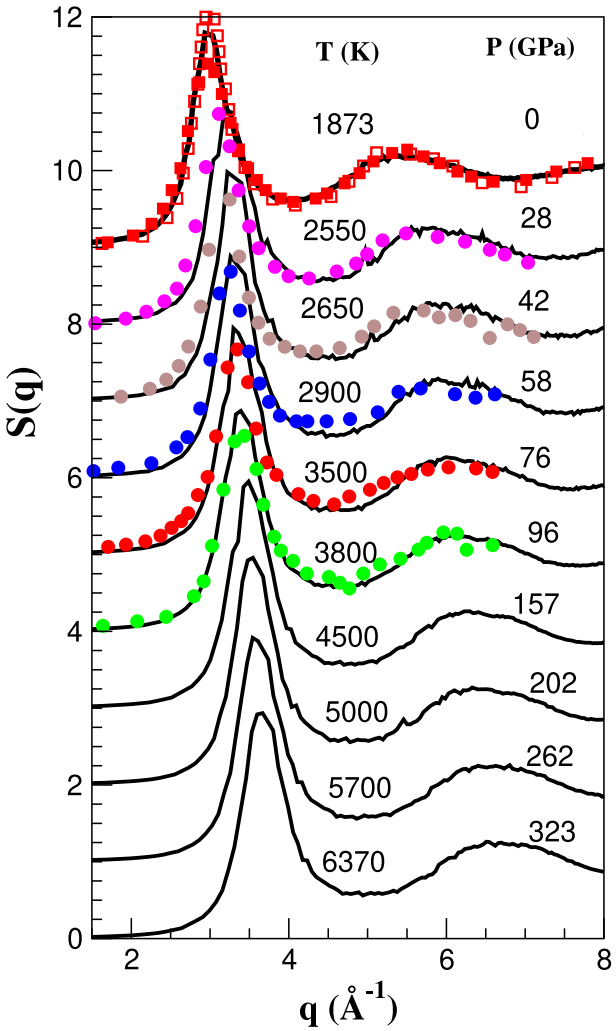

Figure 5. Static structure factor of l-Fe at several high pressures along the melting line. Continuous line: ab-initio molecular dynamics simulations. Open and full squares: experimental X-ray diffraction (XD) data from Inui et al. (2009) and neutron diffraction data from Shen et al. (2004). Full circles: XD data from Kuwayama et al. (2020) at $P = 21.5$, 40.7, 52.7, 73.8, and 106.3 GPa.

of the self-diffusion values has been obtained by Jakse and Bryk (2019) in an AIMD study of liquid Al along its melting line up to 300 GPa.

With respect to those thermodynamic states characteristic of the LOC, the present AIMD simulations predict a slow increase of D within the range $\sim 0.34 - 0.43$ Å^2/ps when the pressure and temperature vary in the range 157–323 GPa and 4500–6370 K respectively. These results are analogous, although smaller in value, to those obtained, for a similar pressure-temperature range, by the CMD simulations of Fomin et al. (2013) which yielded a range $\sim 0.40 - 0.55$ Å^2/ps and also the AIMD simulations of Alfe et al. (1999) who reported values within the range $\sim 0.40 - 0.60$ Å^2/ps.

The Fourier transform (FT) of $Z(t)$ gives the associated power spectrum, $Z(\omega)$, which accounts for the vibrational density of states of the system (Guarini et al., 2017). This magnitude has been found to play an important role in the understanding of the whole dynamics of liquids due to the close link between the shape of the $Z(\omega)$ and the collective mode frequencies (Guarini et al., 2017). We will later return to this point but now we focus on the shape of the calculated $Z(\omega)$ which are plotted in Figure 6 for the whole pressure range. At ambient pressure, the associated $Z(\omega)$ shows a peak followed by a shoulder, whereas at higher pressures these two features become more separated and move toward greater frequencies, with the shoulder evolving into another peak.

Recent ab-initio studies of l-Na, l-Al, l-Pb, and l-In over a wide range of pressure and temperature conditions (Bryk et al., 2019, 2020; Jakse & Bryk, 2019), have unveiled the existence of a correlation between the appearance of a high frequency shoulder/peak in the $Z(\omega)$ and the emergence (in the transverse dispersion relation) of a second high-frequency transverse branch with a frequency very similar to that of the peak/shoulder. We will analyze this point in the following section where we have evaluated the longitudinal and transverse currents.

3.2.2. Collective Dynamics

The dynamics of density fluctuations are described by the intermediate scattering function, $F(q, t)$, which is defined as

$$F(q,t) = \frac{1}{N}\left\langle \left(\sum_{i=1}^{N} e^{-i\vec{q}\vec{R}_i(t+t_0)}\right)\left(\sum_{j=1}^{N} e^{i\vec{q}\vec{R}_j(t_0)}\right)\right\rangle \tag{2}$$

where $\vec{R}_j(t_0)$ is the position of the jth ion at time t_0. Note that the terms in parenthesis are the Fourier components for the microscopic number density at different times separated by a time interval t. Because of the isotropy of the liquid, this function depends only on $q \equiv |\vec{q}|$, and also note that the initial value reduces to $F(q, t = 0) = S(q)$.

The frequency spectrum of $F(q, t)$ is the dynamic structure factor, $S(q, \omega)$, which is experimentally accessible from the coherent scattered intensity in inelastic X-ray or neutron scattering experiments. The current due to the collective motion of the particles, $\vec{j}(q, t)$, is defined as

$$\vec{j}(q,t) = \sum_{i=1}^{N} \vec{v}_i(t) \exp\left[i\vec{q}\cdot\vec{R}_i(t)\right]. \tag{3}$$

This vector can be split into two components, a longitudinal one, $\vec{j}_l(q, t)$, parallel to $\vec{q}$, and a transverse one, $\vec{j}_t(q, t)$, perpendicular to $\vec{q}$. We denote their autocorrelation functions by

$$C_l(q,t) = \frac{1}{N}\langle j_l(q, t + t_0) j_l^*(q, t_0)\rangle \tag{4}$$

Table 3
Calculated Values of S(0), Isothermal Compressibility κ_T, Adiabatic Sound Velocity (c_s) and Velocity of the Transverse Waves (c_t) for the Different States

P (GPa)	$S(0)$	κ_T (10^{-11} Pa^{-1})	c_s (m/s)	c_t (m/s)
0	0.0220 ± 0.002	1.24 ± 0.11	3,950 ± 150	2,200 ± 100
28	0.0140 ± 0.002	0.41 ± 0.06	5,875 ± 325	2,320 ± 100
42	0.0110 ± 0.001	0.30 ± 0.03	6,575 ± 375	2,370 ± 100
58	0.0105 ± 0.001	0.249 ± 0.024	6,825 ± 400	2,540 ± 150
76	0.0100 ± 0.001	0.190 ± 0.019	7,225 ± 425	2,640 ± 150
96	0.0095 ± 0.001	0.162 ± 0.017	7,680 ± 475	2,790 ± 150
157	0.0090 ± 0.001	0.119 ± 0.013	8,550 ± 550	3,160 ± 200
202	0.0085 ± 0.001	0.096 ± 0.011	9,090 ± 600	3,370 ± 200
262	0.0085 ± 0.001	0.080 ± 0.009	9,600 ± 650	3,670 ± 250
293	0.0080 ± 0.001	0.068 ± 0.008	9,950 ± 675	4,050 ± 250
323	0.0080 ± 0.001	0.065 ± 0.008	10,150 ± 700	4,160 ± 250

and

$$C_t(q,t) = \frac{1}{2N}\langle \vec{j}_t(q,t+t_0)\cdot \vec{j}_t^{*}(q,t_0)\rangle, \tag{5}$$

respectively. Their FT into the frequency domain give the corresponding spectra $C_l(q, \omega)$ and $C_t(q, \omega)$.

The calculated normalized intermediate scattering functions, $F(q, t)/S(q)$, are shown in Figure 7 for several pressures. The obvious oscillations for small q-values signal the propagation of density fluctuations (i.e., sound propagation) whose frequency and attenuation both increase initially with increasing q. Further increase in the wavevector leads to a decrease in the frequency of the oscillations, while the attenuation continues to increase, leading to a very slow decay of $F(q, t)$ at $q \approx q_p$, which is the well-known de Gennes' slowing-down effect, related to the strong spatial correlations occurring at these wavevectors. For a fixed q/q_p value, when the pressure is increased, the frequency of the oscillations in the $F(q, t)$ is also enhanced, and this implies that the associated adiabatic sound velocity increases with pressure.

The theoretical analysis of the mechanisms that rule the collective dynamics is usually performed not on $F(q, t)$ directly, but rather on its second order memory function, $N(q, t)$ (Balucani & Zoppi, 1994). For instance, in the hydrodynamic regime (very small q) this latter function contains an instantaneous decay term related to viscous relaxation, and a term that decays more slowly, related to thermal relaxation. At larger q it is customary to consider instead two exponentially decaying relaxation terms, a faster one and a slower one.

$$N(q,t) = A_s(q)e^{-t/\tau_s(q)} + A_f(q)e^{-t/\tau_f(q)} \tag{6}$$

where $\tau_s(q)$ and $\tau_f(q)$ are slow and fast relaxation times and $A_s(q)$ and $A_f(q)$ their corresponding amplitudes. However there are two possible interpretations about which term is the slow one, either the thermal relaxation (as in the hydrodynamic regime) which is therefore called the generalized hydrodynamic model, or the viscous one, which is usually called a viscoelastic model. We have fitted the AIMD obtained $N(q, t)$ to Equation 6 to obtain the fast and slow amplitudes and relaxation times, and analyzed their behavior as a function of q. In particular we have evaluated the generalized heat capacity ratio, $\gamma(q)$, which in the $q \to 0$ limit yields the thermophysical value γ_0, that is, the ratio between specific heats at constant pressure and constant volume (see Ref. (Bryk & Mryglod, 2000, 2001a, 2001b; Calderin et al., 2009, 2011, 2013; Canales et al., 1994)). The expression for $\gamma(q)$ has a different functional dependence on the $A_s(q)$ depending on the model, so for each q we have derived two values for $\gamma(q)$, namely, $\gamma_{\rm th}(q)$, which corresponds to the generalized hydrodynamic, and $\gamma_v(q)$, which would be the correct one if the generalized viscoelastic model applies.

Figure 8 depicts the results obtained for both models at $P = 0$, 58 and 323 GPa along with the "experimental" data for l-Fe at ambient pressure, measured by Hosokawa et al. (2008). These were obtained from the ratio between the intensities of the quasielastic and inelastic lines in the IXS experiments, which is fact an approximation for q values outside the hydrodynamic regime. The data for $\gamma_{\rm exp}(q)$ are somewhat noisy in the low q region, but it can be

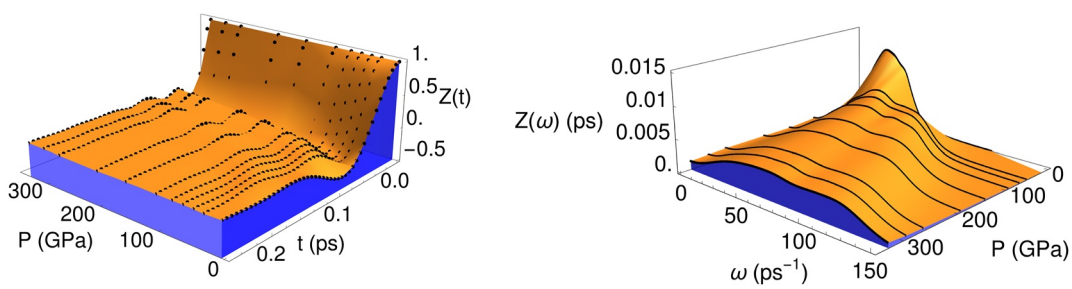

Figure 6. Normalized velocity autocorrelation function (left panel) and its power spectrum (right panel) for l-Fe at several pressures along the melting line.

Table 4
Calculated Values of the Self-Diffusion Coefficients (D), Einstein Frequencies (ω_E) and Shear Viscosity (η) for the Different States

P (GPa)	D (Å^2/ps)	ω_E (ps^{-1})	η (GPa ps)
0	0.320 ± 0.02	32.4	5.70 ± 0.30
28	0.260 ± 0.03	47.2	8.10 ± 0.30
42	0.220 ± 0.03	51.2	11.4 ± 0.30
58	0.212 ± 0.03	54.7	11.9 ± 0.30
76	0.320 ± 0.03	57.5	11.0 ± 0.40
96	0.335 ± 0.03	60.4	11.4 ± 0.40
157	0.340 ± 0.03	69.6	12.1 ± 0.50
202	0.350 ± 0.03	74.9	12.5 ± 0.50
262	0.380 ± 0.03	82.2	12.9 ± 0.50
293	0.420 ± 0.03	84.9	13.1 ± 0.50
323	0.450 ± 0.03	87.4	13.5 ± 0.50

observed that $\gamma_{exp}(q)$ decreases in this q range and approaches unity beyond $q/q_p \approx 0.5$. The interpolating line suggested by Hosokawa et al. (2008), points to $\gamma_{exp}(q \to 0) \equiv \gamma_0 \approx 1.60 - 1.80$, which compares well with other semiempirical values derived from other thermophysical magnitudes, that is, $\gamma_0 = 1.80$ (Iida et al., 2006), 1.57 (Blairs, 2007), and 1.62 (Ayrinhac, 2021). Regarding our calculated results we remark three aspects: (a) $\gamma_v(q)$ is always larger than $\gamma_{th}(q)$, (b) the values of $\gamma(q)$ for both models decrease with increasing pressure, and (c) the $\gamma_v(q)$ are monotonically increasing functions of q, whereas $\gamma_{th}(q)$ initially decrease, coming close to unity when $q/q_p \approx 0.5$. Comparison with the "experimental" $\gamma_{exp}(q)$ at ambient pressure, shows that our calculated $\gamma_{th}(q)$ follow a similar qualitative behavior, which suggests that the generalized hydrodynamic model might be more appropriate for describing the microscopic dynamics of l-Fe in the whole pressure range. Note, moreover, that the decrease with pressure of the $\gamma(q)$ functions is in qualitative agreement with the semiempirical results for the pressure dependence of γ_0 in l-Fe, which indicate that γ_0 decreases with increasing pressure approaching a value of unity for very high pressure (Ayrinhac, 2021). For comparison, the semiempirical expression of Ayrinhac (2021) gives for l-Fe at 28 GPa and 2560 K an estimate $\gamma_0 \approx 1.15$. We note that the present results follow a similar trend to those previously obtained for $\gamma_v(q)$ and $\gamma_{th}(q)$ in liquid Li, Bi, Pb, Hg, and Cd (Bryk & Mryglod, 2000, 2001a, 2001b; Calderin et al., 2009, 2011, 2013; Canales et al., 1994).

The dynamic structure factors have been obtained by a numerical time FT (after application of a window function) of the $F(q, t)$, and Figure 9 show the calculated $S(q, \omega)/S(q)$ for several pressures. No IXS experiments have been performed yet at high pressures, but we remind that a previous AIMD study of l-Fe at ambient pressure (Marques et al., 2015) gave results in good agreement with the IXS data of Hosokawa et al. (2008). Clear side peaks are observed in Figure 9 for all the pressures up to $q \approx (4/5)q_p$, indicative of propagating collective density excitations, with a visible dispersion relation, $\omega_m(q)$, that has been pictured in Figure 10 for several additional pressures.

We have estimated the adiabatic sound velocity, c_s, from the slope of $\omega_m(q)$ at small q, which has been obtained from a linear fit of the obtained dispersion relations. The results are given in Table 3. We note that for ambient pressure this AIMD method yielded a value $c_{s,AIMD} \approx 3{,}950 \pm 150$ m/s which is close to the experimental data of $c_{s,exp} \approx 3{,}820 \pm 150$ m/s (Nasch et al., 1994). The obtained values for higher pressures are subject to a larger uncertainty due to the increase in the minimum value of q available for the simulation and are estimated to

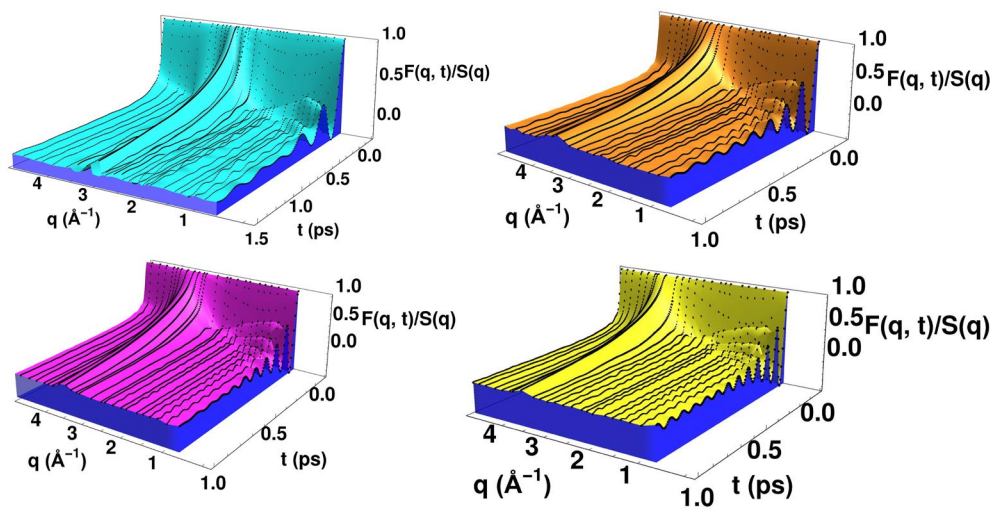

Figure 7. Normalized intermediate scattering function, $F(q, t)/S(q)$, of l-Fe at several pressures. Top left: ambient pressure. Top right: 100 GPa. Bottom left: 200 GPa. Bottom right: 323 GPa.

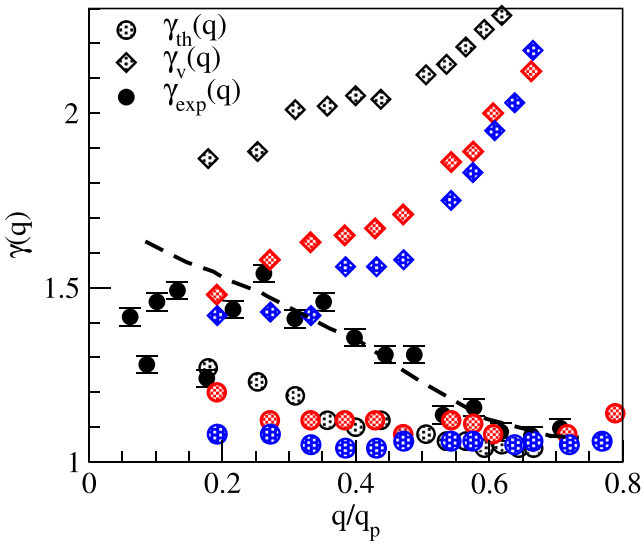

Figure 8. Generalized specific heat ratio, $\gamma(q)$, as obtained from either the generalized hydrodynamic model (circles) or the generalized viscoelastic one (lozenges). The gray, red and blue symbols correspond to $P = 0$, 58, and 323 GPa respectively. The full circles with error bars are experimental inelastic X-ray scattering data of Hosokawa et al. (2008) at ambient pressure and the dashed line an interpolating formula proposed by the same authors (Hosokawa et al., 2008).

increase roughly from a 4% to a 7% from ambient up to the highest pressure considered. These sound velocities are plotted Figure 10 along with measurements of shock-compressed l-Fe at Earth-core conditions (Brown & McQueen, 1986; Nguyen & Holmes, 2004). We observe a good agreement in the pressure region where shock experiments correspond to molten Fe.

We consider now the spectra of the longitudinal and transverse current correlation functions, which have been obtained by (windowed) numerical FT of the corresponding $C_l(q, t)$ and $C_t(q, t)$. The $C_l(q, \omega)$ show for all pressures a similar behavior, with a single maximum at a frequency $\omega_l(q)$, which defines a longitudinal dispersion relation that has been plotted in Figure 11 for the whole pressure range considered in this paper.

Shear waves cannot be sustained macroscopically by a liquid, and this implies that the transverse current spectrum, $C_t(q, \omega)$, decays monotonically with ω at very small q. However, with increasing wavevectors, an elastic component starts to appear and at some point, after a propagation gap, q_t, shear waves do show up and $C_t(q, \omega)$ displays a peak at a non-zero frequency, $\omega_t(q)$. We have found that for all pressures considered in this work the corresponding $C_t(q, \omega)$ already showed a peak at the smallest attainable q, that is, $q_{\min}$, which indicates that $q_t \leq q_{\min}$. In the region of q-values slightly greater than q_t the shape of the dispersion relation has been well described by a viscoelastic model (Balucani & Zoppi, 1994; del Rio & Gonzalez, 2014; Marques et al., 2015) and it has an almost linear behavior, so we have evaluated its slope in order to attain an estimate for the velocity of the associated transverse waves near the onset of their appearance. Moreover, we have found that for q greater than 0.5 q_p, the $C_t(q, \omega)$ display, within a limited q-range, another, higher frequency peak, $\omega_t^h(q)$, whose q-region of existence widens with increasing pressure, evolving from a range [0.75 q_p, 0.95 q_p] at ambient pressure to [0.55 q_p – 1.15 q_p] at 323 GPa. All these features are displayed in Figure 11, where we have plotted the dispersion relations for the transverse low-frequency ($\omega_t(q)$) and high-frequency ($\omega_t^h(q)$) collective modes. The existence of two transverse dispersion branches has also been found in other liquid metals at both high (Li, Na, Al, and Pb (Bryk et al., 2019; Jakse & Bryk, 2019)) and ambient pressures (Tl, Pb, V, Cr, Co, Ni (Bryk et al., 2019; del Rio, Pascual, Gonzalez, & Gonzalez, 2020; del Rio, Pascual, Rodriguez, et al., 2020)). The

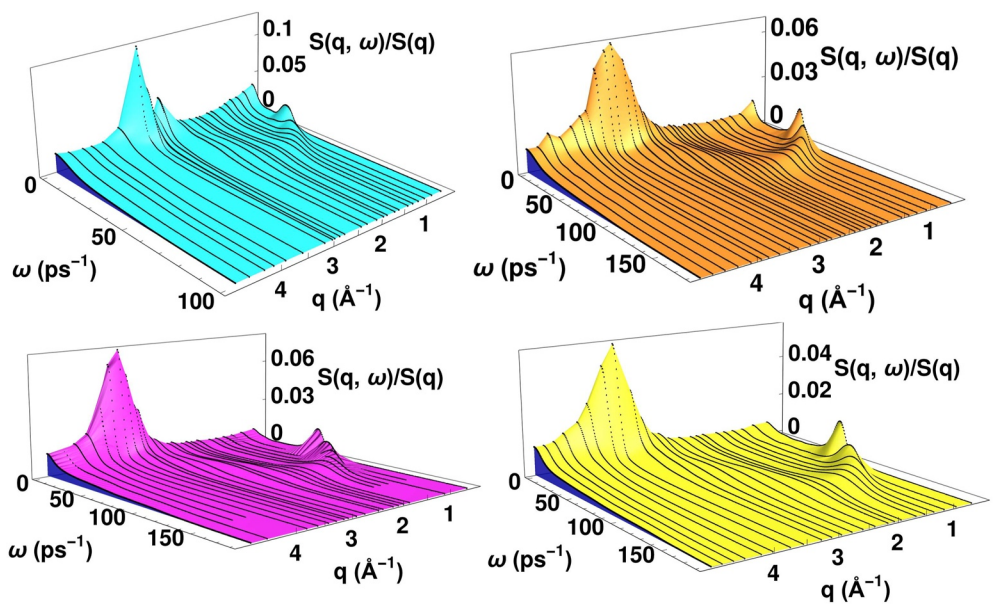

Figure 9. Dynamic structure factor, $S(q, \omega)/S(q)$ in ps units, of l-Fe at several pressures. Top left: ambient pressure. Top right: 100 GPa. Bottom left: 200 GPa. Bottom right: 323 GPa.

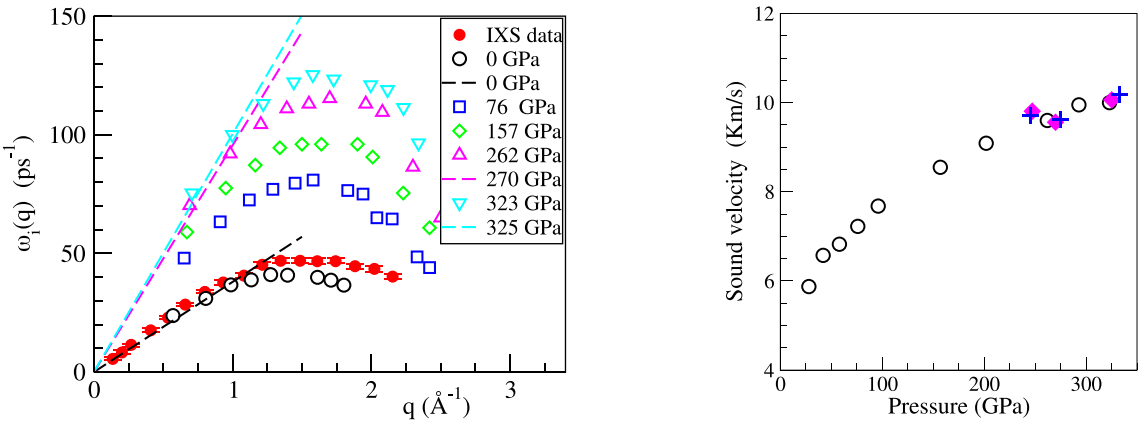

Figure 10. Left panel: dispersion relation of $S(q, \omega)$ for l-Fe at several pressures. Dashed lines: linear dispersion with the experimental hydrodynamic sound velocity, 3,820 m/s, at ambient pressure (Nasch et al., 1994) and as obtained from shock experiments (Brown & McQueen, 1986; Nguyen & Holmes, 2004). Right panel: Pressure-velocity relation for liquid iron. Circles: Present ab-initio molecular dynamics results. Pluses and diamonds: Shock experiments (Brown & McQueen, 1986; Nguyen & Holmes, 2004).

origin of the two transverse branches (high- and low frequency) has been explained in terms of mode-coupling ideas (del Rio & Gonzalez, 2017; del Rio et al., 2018) where the double mode structure in the $C_t(q, \omega)$ is justified by a coupling of the transverse current with density fluctuations at all wave vectors.

It has been recently observed (Bryk et al., 2019, 2020; Jakse & Bryk, 2019), in the study of several systems over a wide pressure range, that the high and low peak frequencies of $Z(\omega)$ remarkably coincide with those in the quasi-flat region of the dispersion relations of $C_t(q, \omega)$, and both show a linear variation in terms of the density, with the low frequency peaks showing a smaller slope. In Figure 12, we show that the same picture continues to be valid also for l-Fe.

The viscosity of l-Fe is an important parameter in order to model and understand some fundamental processes taking place in the LOC, such as the generation of the Earth's magnetic field. From the AIMD obtained $C_t(q, t)$, we have evaluated the corresponding shear viscosity coefficient η according to the method described in Refs (Balucani et al., 2000; L. E. Gonzalez & Gonzalez, 2008; D. J. Gonzalez et al., 2001, D. J. Gonzalez et al., 2002; Blanco et al., 2003). The results obtained are given in Table 4. Comparison with experiment can only be made at ambient pressure for which the present AIMD result $\eta_{\mathrm{AIMD}} = 5.70 \pm 0.30$ GPa ps is close to the experimental data $\eta_{\mathrm{exp}} \approx 5.20 \pm 0.05$ (Assael et al., 2006), 5.30 GPa ps (Shimoji & Itami, 1986). As for the other high pressure and temperature states and more specifically those characteristic of the LOC, namely $157 \leq P \leq 323$ GPa and $4500 \leq T \leq 6370$ K, the present AIMD results show a very small variation, namely $12.0 \leq \eta_{\mathrm{AIMD}} \leq 13.5$ GPa ps. This range of values is similar, although narrower, to the range yielded by the CMD results of Fomin et al. (2013) ($6.0 \leq \eta_{\mathrm{CMD}} \leq 12.0$ GPa ps) and the AIMD results of Alfe et al. (1999) ($8.0 \leq \eta_{\mathrm{AIMD}} \leq 15.0$ GPa ps).

The estimation of the shear viscosity in the context of MD simulations has sometimes been carried out by resorting to the Stokes-Einstein (SE) formula $\eta D = k_B T/2\pi d$, which connects the self-diffusion coefficient D of a

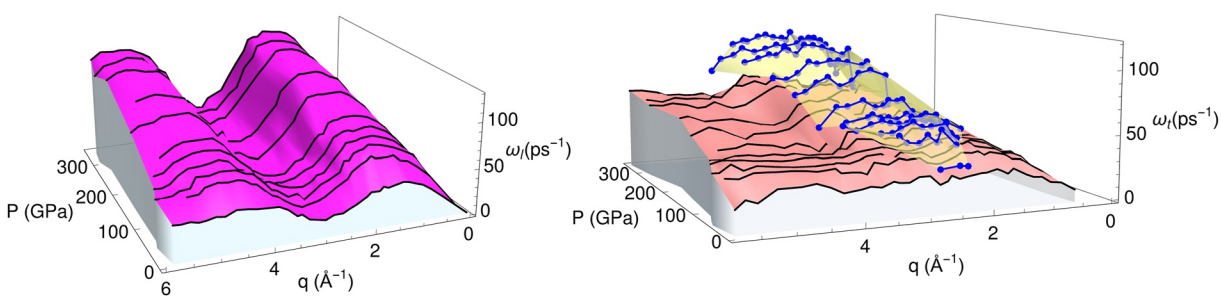

Figure 11. Longitudinal (left panel) and transverse (right panel) dispersion relations, for l-Fe at several pressures, obtained from the positions of the peaks in the spectra $C_l(q, \omega)$ and $C_t(q, \omega)$ respectively. In the right panel lines denote the low-frequency modes $\omega_t(q)$, and lines with dots the high-frequency modes $\omega_t^h(q)$

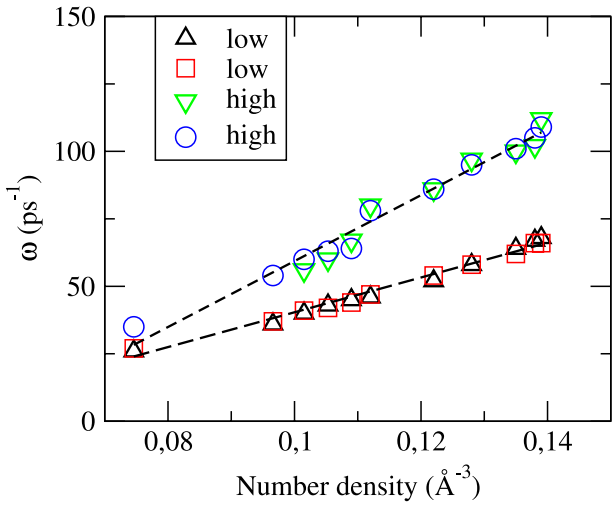

Figure 12. Low and high frequency peaks of $Z(\omega)$ (triangles up and down) and of $C_l(q, \omega)$ (squares and circles) as a function of density.

macroscopic particle of diameter d with the shear viscosity, η, of the liquid in which the particle moves. Although the SE formula is not intended for atoms, it has often been used when dealing with liquid metals in order to evaluate η in terms of D and d (which is taken as r_p, the position of the main peak of $g(r)$). This has been prompted by the fact that the calculation of the shear viscosity in AIMD simulations requires long simulations in order to attain useful statistical accuracy whereas significantly shorter simulations are needed for the self-diffusion coefficient. However, given its uncertain validity when dealing with atomic diffusion, we have checked if the SE formula is reliable within the wide pressure range considered in this work. We have used our AIMD results for both η and D in order to compare their product with the factor on the right hand side of the SE formula. The results are plotted in Figure 13 where it is observed that the SE relation holds rather well up to a pressure ≈100 GPa, but with increasing pressure clear differences become more noticeable.

The last point we want to discuss related to transverse currents is its possible appearance in the dynamic structure factor and/or in the spectra of the longitudinal current correlation functions as small peaks or shoulders near the frequencies $\omega_t(q)$. Such a possibility was originally suggested in an IXS measurement of the $S(q, \omega)$ in l-Ga (Hosokawa et al., 2009), which was also backed by some ab initio simulations. Since then, this kind of signature of TA modes in the longitudinal signals, either $S(q, \omega)$ or $C_l(q, \omega)$, have been observed for several other liquid metals at ambient pressure (Hosokawa, Munejiri, Inui, Kajihara, Pilgrim, Baron, 2013; Hosokawa, Munejiri, Inui, Kajihara, Pilgrim, Ohmasa, 2013, Hosokawa et al., 2015; Munejiri et al., 2012). In the case of $S(q, \omega)$ those features become visible in a narrow range of wavevectors around $q_p/2$, and in a frequency region near the minimum that separates the quasielastic and inelastic lines.

In a previous AIMD study of l-Fe at ambient and some high pressure states (Marques et al., 2015, 2016), we also observed the same type of TA excitation modes in $S(q, \omega)$. We have now extended this analysis to the present high pressure/temperature states. The results are depicted in Figure 14 which shows the calculated $S(q, \omega)$ for some high pressure states, and we observe that these features do appear within the range of wavevectors, approximately, $0.27 \leq q/q_p \leq 0.38$, but become weaker with increasing pressure. In fact, for pressures greater than ≈200 GPa there is only a weak feature for $q/q_p = 0.27$. In Figure 14, we have also marked the energies associated with the peak positions of the transverse current spectra; this hints to its interpretation as TA excitation modes.

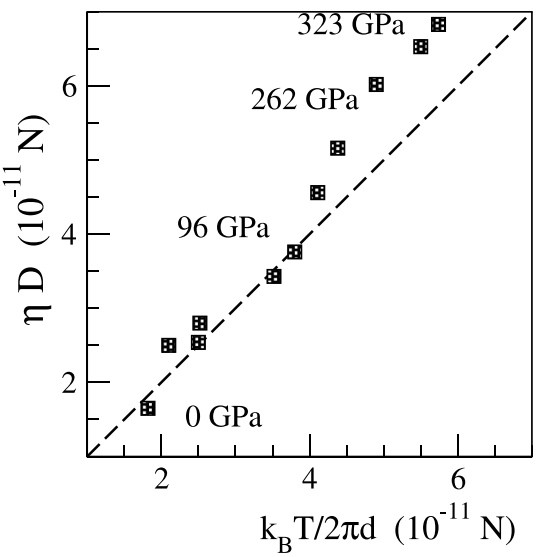

Figure 13. Stokes-Einstein relation for the thermodynamics states considered in this work.

3.3. Electronic Properties

We have also calculated the total electronic density of states. This was obtained from the self-consistent eigenvalues and was averaged over four ionic configurations with a time separation of ≈6–10 ps and sampling over a 6 by 6 by 6 mesh of points in the Brillouin zone.

The obtained results are plotted in Figure 15, where we observe that the position of the Fermi level points to a metallic behavior throughout the whole explored pressure range. With increasing pressure there is a broadening of the conduction band.

We finally note that the spin polarization is important for the lower pressure states, but it becomes negligible for P above 42 GPa, and for this reason it was directly discarded in the simulations for higher pressures, as mentioned in Section 2.

4. Conclusions

We have performed an ab initio simulation study on the static and dynamic properties of l-Fe along its melting curve up to a temperature and pressure of 6370 K and 323 GPa respectively.

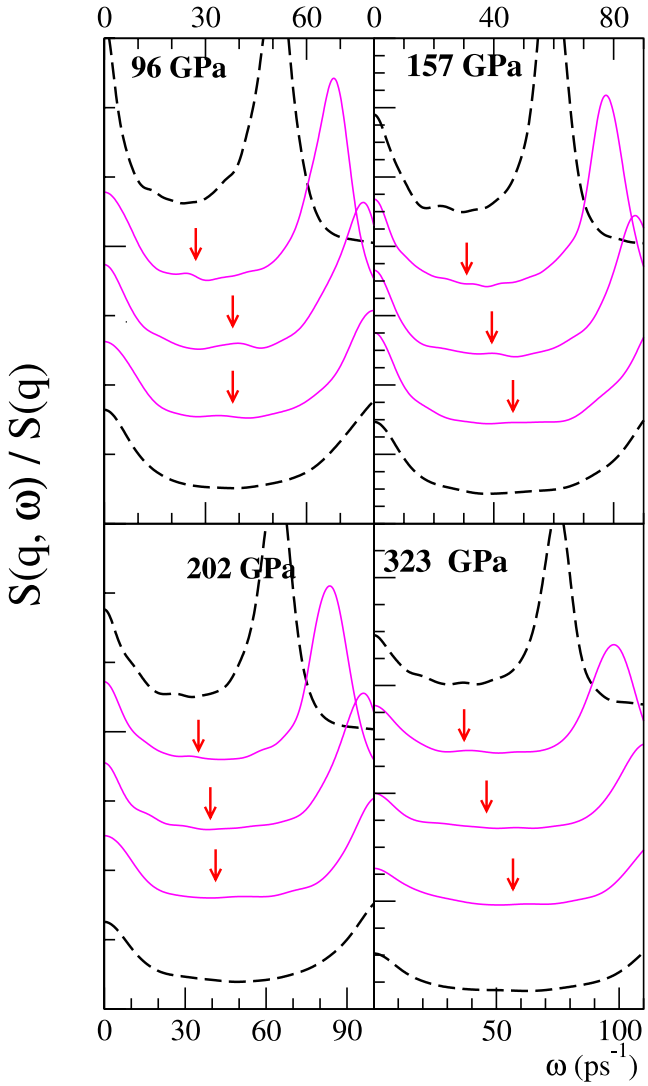

Figure 14. Dynamic structure factors, $S(q, \omega)/S(q)$, for l-Fe at $P = 96$, 157, 202, and 323 GPa and $q/q_p = 0.19$, 0.27, 0.33, 0.38, and 0.43 (top to bottom). The vertical scales are offset for clarity, and the arrows mark the frequencies of the transverse acoustic modes, $\omega_t(q)$.

The calculated static structure agrees well with the available experimental data. The $S(q)$ display, up to ≈200 GPa, an asymmetric shape in its second peak, which can be connected to the appearance of a significant amount of icosahedral short-range order. On the other hand, the number of NNs remains practically constant (≈12.6) over the whole pressure/temperature range whereas the reduced averaged interatomic distances exhibit some variations within the pressure range up to ≈100 GPa only.

The calculated VACF functions show the typical oscillatory behavior with a first minimum whose position moves to shorter times with increasing pressure. From its time integral we have evaluated the associated self-diffusion coefficients whose pressure dependence shows a non-monotonic behavior reaching a minimum value at ≈58 GPa and therefrom it smoothly increases. The power spectrum of the VACF function, $Z(\omega)$, shows at low pressures a peak followed by a shoulder and with growing pressure their associated frequencies increase and the shoulder evolves into another peak.

The dynamic structure factors, $S(q, \omega)$, show side-peaks, indicative of propagating density excitations, up to $q \approx (4/5)\, q_p$. The associated dispersion relation has been used to estimate the adiabatic sound velocity along the melting curve. Comparison with measurements of shock-compressed l-Fe reveals a fair agreement which improves with increasing pressure. Moreover, the $S(q, \omega)$ show, for $q \leq 0.5\ q_p$, the same type of TA excitation modes that were detected in l-Fe at ambient conditions, but with a strength that weakens with increasing pressure.

The collective dynamics has also been investigated through the calculation of the longitudinal and transverse currents, their spectral functions and the corresponding dispersion relations. For all states, the transverse dispersion relation shows two branches with the high frequency branch appearing over a limited q-range. Moreover, we have found a correlation between the frequencies of both transverse branches and the low and high frequency peaks in the corresponding $Z(\omega)$.

The results for the shear viscosity show a non-monotonic pressure dependence but in the pressure/temperature range of the LOC, it shows a smooth increase. Using the obtained AIMD results for the self-diffusion and shear viscosity coefficients we have also analyzed the accuracy of the SE formula. It was found that this relation holds rather well up to pressures smaller than ≈100 GPa, but for greater pressures it gradually becomes less reliable.

Finally, we want to discuss two points related to the reliability of the results presented, namely, their dependence on the parameters of the simulations, and the uncertainty about the thermodynamic stability of the samples.

To test the first point we have performed some checks in order to assess the dependence of the results on some of the parameters of the simulations. Specifically, we have carried out additional AIMD simulation calculations intended to analyze the influence of the number of particles used in the simulation box, the number of k-points used in the Brillouin zone sampling, the number of valence electrons in the ionic pseudopotential and the ionic time step. These additional runs were performed for the states corresponding to 202 and 323 GPa. For the 202 GPa state, we carried out three different AIMD calculations. One calculation considered a larger system (150 particles), another calculation had a higher number of k-points (eight k-points) and the third calculation was performed using an ionic pseudopotential that includes also the atomic 3s electrons as valence electrons (a total of 16 valence electrons). The obtained results for the $g(r)$ and $S(q)$ were practically identical to the corresponding ones reported in Figures 2 and 5. The new values of the associated transport coefficients, namely D, c_s and η, were within a 12% range of the values reported in Table 4. For the 323 GPa state, we performed an AIMD simulation using a larger simulation sample (150 particles), an ionic pseudopotential with 16 valence electrons and a smaller

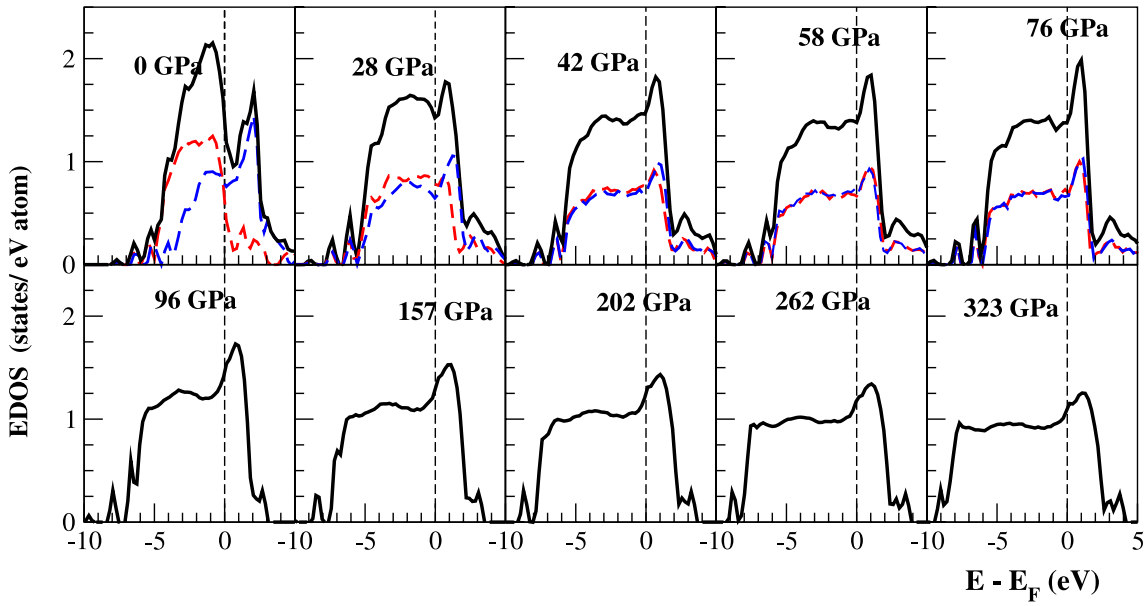

Figure 15. Pressure dependence of the total electronic density of states (EDOS). The decomposition of the EDOS into the spin up (red dashed line) and spin down (blue dashed line) contributions is also shown for the lower pressure states.

ionic timestep (1 fs). Again, the new results for the $g(r)$ and $S(q)$ were practically identical to those reported in Figures 2 and 5. As for the transport coefficients, the changes were smaller than 10% of those reported in Table 4.

Concerning the second point, we cannot guarantee that the liquid samples that we have obtained in our simulations correspond to a thermodynamically stable phase. We have tried to play on the safe side by selecting for each pressure a temperature slightly higher than the melting temperature provided by previous thermodynamic calculations (Alfe et al., 1999, 2002) that used a similar level of DFT theory as the one we have used here. Nevertheless in those calculations the possibility of a stable BCC phase was not taken into account, and consequently the corresponding melting temperature may be incorrect. If that were the case, it may happen that the temperatures of our simulations were below the correct (thermodynamic) melting temperature and our liquids would be in fact somewhat undercooled in the region of pressures above 150 GPa. Therefore the question may be raised about how the results would change upon increasing the temperature (in order to surpass the melting temperature). Based on general grounds, we would expect minor changes in structural magnitudes which would involve slightly wider and lower peaks in $g(r)$ and $S(q)$, but no changes in positions, or abundances of different types of local ordering. Concerning transport properties, one may expect slightly higher diffusion coefficients and sound velocities, and slightly lower viscosities. Nevertheless, the pressure variation of all the properties reported would not change qualitatively, and the variations produced by an increase in temperature would not modify the general picture obtained in this study.

Data Availability Statement

All the data reported in this work can be accessed at the following repository of the University of Valladolid: https://uvadoc.uva.es/handle/10324/54118.

Acknowledgments
We acknowledge the support of the Spanish Ministry of Economy and Competitiveness in conjunction with the European Regional Development Fund (Project PGC2018-093745-B-I00).

References

Alfe, D. (2009). Temperature of the inner-core boundary of the Earth: Melting of iron at high pressure from first-principles coexistence simulations. *Physical Review B: Condensed Matter*, *79*(6), 060101. https://doi.org/10.1103/PhysRevB.79.060101

Alfe, D., Gillan, M. J., & Price, G. D. (1999). The melting curve of iron at the pressures of the Earth's core from ab initio calculations. *Nature*, *401*(6752), 462–464. https://doi.org/10.1038/46758

Alfe, D., Kresse, G., & Gillan, M. J. (2000). Structure and dynamics of liquid iron under Earth's core conditions. *Physical Review B: Condensed Matter*, *61*(1), 132–142. https://doi.org/10.1103/PhysRevB.61.132

Alfe, D., Price, G. D., & Gillan, M. J. (2002). Iron under Earth's core conditions: Liquid-state thermodynamics and high-pressure melting curve from ab initio calculations. *Physical Review B: Condensed Matter*, *65*(16), 165118. https://doi.org/10.1103/PhysRevB.65.165118

Alfe, D., Price, G. D., & Gillan, M. J. (2004). The melting curve of iron from quantum mechanics calculations. *Journal of Physics and Chemistry of Solids*, *65*(8–9), 1573–1580. https://doi.org/10.1016/j.jpcs.2003.12.014

Anderson, W. W., & Ahrens, T. J. (1994). An equation of state for liquid-iron and implications for the Earth's core. *Journal of Geophysical Research*, *99*(B3), 4273–4284. https://doi.org/10.1029/93JB03158

Anzellini, S., Dewaele, A., Mezouar, M., Loubeyre, P., & Morard, G. (2013). Melting of iron at Earth's inner core boundary based on fast X-ray diffraction. *Science*, *340*(6131), 464–466. https://doi.org/10.1126/science.1233514

Assael, M. J., Kakosimos, K., Banish, R. M., Brillo, J., Egry, I., Brooks, R., et al. (2006). Reference data for the density and viscosity of liquid aluminum and liquid iron. *Journal of Physical and Chemical Reference Data*, *35*(1), 285–300. https://doi.org/10.1063/1.2149380

Ayrinhac, S. (2021). Heat capacity ratio in liquids at high pressure. *Journal of Applied Physics*, *129*(18), 185903. https://doi.org/10.1063/5.0037101

Balucani, U., Brodholt, J. P., Jedlovszky, P., & Vallauri, R. (2000). Viscosity of liquid water from computer simulations with a polarizable potential model. *Physical Review E - Statistical Physics, Plasmas, Fluids, and Related Interdisciplinary Topics*, *62*(2B), 2971–2973. https://doi.org/10.1103/PhysRevE.62.2971

Balucani, U., & Zoppi, M. (1994). *Dynamics of the liquid state*. Oxford University Press.

Belonoshko, A. B., Ahuja, R., & Johansson, B. (2000). Quasi—ab initio molecular dynamic study of Fe melting. *Physical Review Letters*, *84*(16), 3638–3641. https://doi.org/10.1103/PhysRevLett.84.3638

Belonoshko, A. B., Arapan, S., & Rosengren, A. (2011). An ab initio molecular dynamics study of iron phases at high pressure and temperature. *Journal of Physics: Condensed Matter*, *23*(48), 485402. https://doi.org/10.1088/0953-8984/23/48/485402

Belonoshko, A. B., Fu, J., & Smirnov, G. (2021). Free energies of iron phases at high pressure and temperature: Molecular dynamics study. *Physical Review B: Condensed Matter*, *104*(10), 104103. https://doi.org/10.1103/PhysRevB.104.104103

Blairs, S. (2007). Review of data for velocity of sound in pure liquid metals and metalloids. *International Materials Reviews*, *52*(6), 321–344. https://doi.org/10.1179/174328007X212490

Blanco, J., Gonzalez, D. J., Gonzalez, L. E., Lopez, J. M., & Stott, M. J. (2003). Collective ionic dynamics in the liquid Na-Cs alloy: An ab initio molecular dynamics study. *Physical Review E - Statistical Physics, Plasmas, Fluids, and Related Interdisciplinary Topics*, *67*(4), 041204. https://doi.org/10.1103/PhysRevE.67.041204

Brown, J. M., & McQueen, R. G. (1986). Phase-transitions, Gruneisen-parameter, and elasticity for shocked iron between 77-GPa and 400-GPa. *Journal of Geophysical Research*, *91*(B7), 7485–7494. https://doi.org/10.1029/JB091iB07p07485

Bryk, T., & Belonoshko, A. B. (2012). Collective excitations in molten iron above the melting point: A generalized collective-mode analysis of simulations with embedded-atom potentials. *Physical Review B: Condensed Matter*, *86*(2), 024202. https://doi.org/10.1103/PhysRevB.86.024202

Bryk, T., Demchuk, T., & Jakse, N. (2019). Atomistic structure and collective dynamics in liquid Pb along the melting line up to 70 GPa: A first-principles molecular dynamics study. *Physical Review B: Condensed Matter*, *99*(1), 014201. https://doi.org/10.1103/PhysRevB.99.014201

Bryk, T., Demchuk, T., Wax, J.-F., & Jakse, N. (2020). Pressure-induced effects in the spectra of collective excitations in pure liquid metals. *Journal of Physics: Condensed Matter*, *32*(18). https://doi.org/10.1088/1361-648X/ab6a31

Bryk, T., De Panfilis, S., Gorelli, F. A., Gregoryanz, E., Krisch, M., Ruocco, G., et al. (2013). Dynamical crossover at the liquid-liquid transformation of a compressed molten alkali metal. *Physical Review Letters*, *111*(7), 077801. https://doi.org/10.1103/PhysRevLett.111.077801

Bryk, T., & Mryglod, I. (2000). Collective excitations in liquid bismuth. *Journal of Physics: Condensed Matter*, *12*(15), 3543–3558. https://doi.org/10.1088/0953-8984/12/15/304

Bryk, T., & Mryglod, I. (2001a). Collective dynamics in liquid lead: Generalized propagating excitations. *Physical Review E - Statistical Physics, Plasmas, Fluids, and Related Interdisciplinary Topics*, *63*(5), 051202. https://doi.org/10.1103/PhysRevE.63.051202

Bryk, T., & Mryglod, I. (2001b). Collective excitations in liquid bismuth: The origin of kinetic relaxing modes. *Journal of Physics: Condensed Matter*, *13*(7), 1343–1352. https://doi.org/10.1088/0953-8984/13/7/301

Calderin, L., Gonzalez, L. E., & Gonzalez, D. J. (2009). Ab initio molecular dynamics study of the static, dynamic, and electronic properties of liquid mercury at room temperature. *Journal of Chemical Physics*, *130*(19), 194505. https://doi.org/10.1063/1.3137582

Calderin, L., Gonzalez, L. E., & Gonzalez, D. J. (2011). Static, dynamic and electronic properties of expanded fluid mercury in the metal-nonmetal transition range. an ab initio study. *Journal of Physics: Condensed Matter*, *23*(37), 375105. https://doi.org/10.1088/0953-8984/23/37/375105

Calderin, L., Gonzalez, L. E., & Gonzalez, D. J. (2013). An ab initio study of the structure and dynamics of bulk liquid cd and its liquid-vapor interface. *Journal of Physics: Condensed Matter*, *25*(6), 065102. https://doi.org/10.1088/0953-8984/25/6/065102

Canales, M., Gonzalez, L. E., & Padro, J. A. (1994). Computer-simulation study of liquid lithium at 470-k and 843-k. *Physical Review E - Statistical Physics, Plasmas, Fluids, and Related Interdisciplinary Topics*, *50*(5), 3656–3669. https://doi.org/10.1103/PhysRevE.50.3656

del Rio, B. G., Chen, M., Gonzalez, L. E., & Carter, E. A. (2018). Orbital-free density functional theory simulation of collective dynamics coupling in liquid Sn. *Journal of Chemical Physics*, *149*(9), 094504. https://doi.org/10.1063/1.5040697

del Rio, B. G., & Gonzalez, L. E. (2014). Orbital free ab initio simulations of liquid alkaline Earth metals: From pseudopotential construction to structural and dynamic properties. *Journal of Physics: Condensed Matter*, *26*(46), 465102. https://doi.org/10.1088/0953-8984/26/46/465102

del Rio, B. G., & Gonzalez, L. E. (2017). Longitudinal, transverse, and single-particle dynamics in liquid Zn: Ab initio study and theoretical analysis. *Physical Review B: Condensed Matter*, *95*(22), 224201. https://doi.org/10.1103/PhysRevB.95.224201

del Rio, B. G., Pascual, C., Gonzalez, L. E., & Gonzalez, D. J. (2020). Structure and dynamics of the liquid 3D transition metals near melting. An ab initio study. *Journal of Physics: Condensed Matter*, *32*(21), 214005. https://doi.org/10.1088/1361-648X/ab6f16

del Rio, B. G., Pascual, C., Rodriguez, O., Gonzalez, L. E., & Gonzalez, D. J. (2020). First principles determination of some static and dynamic properties of the liquid 3d transition metals near melting. *Condensed Matter Physics*, *23*(2), 23606. https://doi.org/10.5488/CMP.23.23606

de Wijs, G. A., Kresse, G., Vocadlo, L., Dobson, D., Alfe, D., Gillan, M., & Price, G. D. (1998). The viscosity of liquid iron at the physical conditions of the Earth's core. *Nature*, *392*(6678), 805–807. https://doi.org/10.1038/33905

Dobson, D. P. (2002). Self-diffusion in liquid Fe at high pressure. *Physics of the Earth and Planetary Interiors*, *130*(3–4), 271–284. https://doi.org/10.1016/S0031-9201(02)00011-0

Dubrovinsky, L. S., Saxena, S. K., Tutti, F., Rekhi, S., & LeBehan, T. (2000). In situ X-ray study of thermal expansion and phase transition of iron at multimegabar pressure. *Physical Review Letters*, *84*(8), 1720–1723. https://doi.org/10.1103/PhysRevLett.84.1720

Fomin, Y. D., Ryzhov, V. N., & Brazhkin, V. V. (2013). Properties of liquid iron along the melting line up to Earth-core pressures. *Journal of Physics: Condensed Matter*, *25*(28), 285104. https://doi.org/10.1088/0953-8984/25/28/285104

Ganesh, P., & Widom, M. (2008). Ab initio simulations of geometrical frustration in supercooled liquid Fe and Fe-based metallic glass. *Physical Review B: Condensed Matter*, *77*(1), 014205. https://doi.org/10.1103/PhysRevB.77.014205

Gillan, M. J., Alfe, D., Brodholt, J., Vocadlo, L., & Price, G. D. (2006). First-principles modelling of Earth and planetary materials at high pressures and temperatures. *Reports on Progress in Physics*, *69*(8), 2365–2441. https://doi.org/10.1088/0034-4885/69/8/R03

Gonzalez, D. J., Gonzalez, L. E., Lopez, J. M., & Stott, M. J. (2001). Orbital free ab initio molecular dynamics study of liquid Al near melting. *Journal of Chemical Physics*, *115*(6), 2373–2376. https://doi.org/10.1063/1.1389473

Gonzalez, D. J., Gonzalez, L. E., Lopez, J. M., & Stott, M. J. (2002). Dynamical properties of liquid Al near melting: An orbital-free molecular dynamics study. *Physical Review B: Condensed Matter*, *65*(18), 184201. https://doi.org/10.1103/PhysRevB.65.184201

Gonzalez, L. E., & Gonzalez, D. J. (2008). Structure and dynamics of bulk liquid Ga and the liquid-vapor interface: An ab initio study. *Physical Review B: Condensed Matter*, *77*(6), 064202. https://doi.org/10.1103/PhysRevB.77.064202

Guarini, E., Bellissima, S., Bafile, U., Farhi, E., De Francesco, A., Formisano, F., & Barocchi, F. (2017). Density of states from mode expansion of the self-dynamic structure factor of a liquid metal. *Physical Review E - Statistical Physics, Plasmas, Fluids, and Related Interdisciplinary Topics*, *95*(1), 012141. https://doi.org/10.1103/PhysRevE.95.012141

Hixson, R. S., Winkler, M. A., & Hodgdon, M. L. (1990). Sound speed and thermophysical properties of liquid-iron and nickel. *Physical Review B: Condensed Matter*, *42*(10), 6485–6491. https://doi.org/10.1103/PhysRevB.42.6485

Hohenberg, P., & Kohn, W. (1964). Inhomogeneous electron gas. *Physical Review*, *136*(3B), B864–B871. https://doi.org/10.1103/PhysRev.136.B864

Honeycutt, J. D., & Andersen, H. C. (1987). Molecular-dynamics study of melting and freezing of small Lennard-Jones clusters. *Journal of Physical Chemistry*, *91*(19), 4950–4963. https://doi.org/10.1021/j100303a014

Hosokawa, S., Inui, M., Kajihara, Y., Matsuda, K., Ichitsubo, T., Pilgrim, W. C., et al. (2009). Transverse acoustic excitations in liquid Ga. *Physical Review Letters*, *102*(10), 105502. https://doi.org/10.1103/PhysRevLett.102.105502

Hosokawa, S., Inui, M., Kajihara, Y., Tsutsui, S., & Baron, A. Q. R. (2015). Transverse excitations in liquid Fe, Cu and Zn. *Journal of Physics: Condensed Matter*, *27*(19), 194104. https://doi.org/10.1088/0953-8984/27/19/194104

Hosokawa, S., Inui, M., Matsuda, K., Ishikawa, D., & Baron, A. Q. R. (2008). Damping of the collective modes in liquid Fe. *Physical Review B: Condensed Matter*, *77*(17), 174203. https://doi.org/10.1103/PhysRevB.77.174203

Hosokawa, S., Munejiri, S., Inui, M., Kajihara, Y., Pilgrim, W. C., Baron, A. Q. R., et al. (2013a). Transverse excitations in liquid metals. In M. Tokuyama & I. Oppenheim (Eds.), *4th international symposium on slow dynamics in complex systems: Keep going Tohoku* (Vol. 1518, pp. 695–702). AMER Institute Physics. https://doi.org/10.1063/1.4794661

Hosokawa, S., Munejiri, S., Inui, M., Kajihara, Y., Pilgrim, W.-C., Ohmasa, Y., et al. (2013b). Transverse excitations in liquid Sn. *Journal of Physics: Condensed Matter*, *25*(11), 112101. https://doi.org/10.1088/0953-8984/25/11/112101

Iida, T., Guthrie, R., & Tripathi, N. (2006). A model for accurate predictions of self-diffusivities in liquid metals, semimetals, and semiconductors. *Metallurgy and Materials Processing Science is Metall Mater Trans B*, *37*(4), 559–564. https://doi.org/10.1007/s11663-006-0039-2

Inui, M., Maruyama, K., Kajihara, Y., & Nakada, M. (2009). Icosahedral ordering in liquid iron studied via X-ray scattering and Monte Carlo simulations. *Physical Review B: Condensed Matter*, *80*(18), 180201. https://doi.org/10.1103/PhysRevB.80.180201

Jakse, N., & Bryk, T. (2019). Pressure evolution of transverse collective excitations in liquid Al along the melting line. *Journal of Chemical Physics*, *151*(3), 034506. https://doi.org/10.1063/1.5099099

Koci, L., Belonoshko, A. B., & Ahuja, R. (2006). Molecular dynamics study of liquid iron under high pressure and high temperature. *Physical Review B: Condensed Matter*, *73*(22), 224113. https://doi.org/10.1103/PhysRevB.73.224113

Kohn, W., & Sham, L. J. (1965). Self-consistent equations including exchange and correlation effects. *Physical Review*, *140*(4A), 1133. https://doi.org/10.1103/PhysRev.140.A1133

Kresse, G., & Furthmuller, J. (1996). Efficient iterative schemes for ab initio total-energy calculations using a plane-wave basis set. *Physical Review B: Condensed Matter*, *54*(16), 11169–11186. https://doi.org/10.1103/PhysRevB.54.11169

Kresse, G., & Joubert, D. (1999). From ultrasoft pseudopotentials to the projector augmented-wave method. *Physical Review B: Condensed Matter*, *59*(3), 1758–1775. https://doi.org/10.1103/PhysRevB.59.1758

Kuwayama, Y., Morard, G., Nakajima, Y., Hirose, K., Baron, A. Q. R., Kawaguchi, S., et al. (2020). Equation of state of liquid iron under extreme conditions. *Physical Review Letters*, *124*(16), 165701. https://doi.org/10.1103/PhysRevLett.124.165701

Marques, M., Gonzalez, L. E., & Gonzalez, D. J. (2015). Ab initio study of the structure and dynamics of bulk liquid Fe. *Physical Review B: Condensed Matter*, *92*(13), 134203. https://doi.org/10.1103/PhysRevB.92.134203

Marques, M., Gonzalez, L. E., & Gonzalez, D. J. (2016). Pressure-induced changes in structural and dynamic properties of liquid Fe close to the melting line. An ab initio study. *Journal of Physics: Condensed Matter*, *28*(7), 075101. https://doi.org/10.1088/0953-8984/28/7/075101

McGreevy, R. L., Baranyai, A., & Ruff, I. (1986). A less arbitrary determination of coordination numbers in disordered-systems. *Physics and Chemistry of Liquids*, *16*(1), 47–54. https://doi.org/10.1080/00319108608078499

Munejiri, S., Shimojo, F., & Hoshino, K. (2012). Static and dynamic structures of liquid tin at high pressure from ab initio molecular dynamics. *Physical Review B: Condensed Matter*, *86*(10), 104202. https://doi.org/10.1103/PhysRevB.86.104202

Nasch, P. M., Manghnani, M. H., & Secco, R. A. (1994). Sound-velocity measurements in liquid-iron by ultrasonic interferometry. *Journal of Geophysical Research*, *99*(B3), 4285–4291. https://doi.org/10.1029/93JB03111

Nguyen, J. H., & Holmes, N. C. (2004). Melting of iron at the physical conditions of the Earth's core. *Nature*, *427*(6972), 339–342. https://doi.org/10.1038/nature02248

Perdew, J. P., Burke, K., & Ernzerhof, M. (1996). Generalized gradient approximation made simple. *Physical Review Letters*, *77*(18), 3865–3868. https://doi.org/10.1103/PhysRevLett.77.3865

Rutter, M. D., Secco, R. A., Liu, H., Uchida, T., Rivers, M. L., Sutton, S. R., & Wang, Y. (2002). Viscosity of liquid Fe at high pressure. *Physical Review B: Condensed Matter*, *66*(6), 060102. https://doi.org/10.1103/PhysRevB.66.060102

Sanloup, C., Guyot, F., Gillet, P., Fiquet, G., Hemley, R. J., Mezouar, M., & Martinez, I. (2000). Structural changes in liquid Fe at high pressures and high temperatures from synchrotron X-ray diffraction. *Europhysics Letters*, *52*(2), 151–157. https://doi.org/10.1209/epl/i2000-00417-3

Schenk, T., Holland-Moritz, D., Simonet, V., Bellissent, R., & Herlach, D. M. (2002). Icosahedral short-range order in deeply undercooled metallic melts. *Physical Review Letters*, *89*(7), 075507. https://doi.org/10.1103/PhysRevLett.89.075507

Secco, R. A., Rutter, M. D., Balog, S. P., Liu, H., Rubie, D. C., Uchida, T., et al. (2002). Viscosity and density of Fe-S liquids at high pressures. *Journal of Physics: Condensed Matter*, *14*(44), 11325–11330. https://doi.org/10.1088/0953-8984/14/44/476

Shen, G., Prakapenka, V. B., Rivers, M. L., & Sutton, S. R. (2004). Structure of liquid iron at pressures up to 58 GPa. *Physical Review Letters*, *92*(18), 185701. https://doi.org/10.1103/PhysRevLett.92.185701

Shimoji, M., & Itami, T. (1986). *Atomic transport in liquid metal*s. Trans-Tech Publications.

Sutton, A. P., & Chen, J. (1990). Long-range Finnis Sinclair potentials. *Philosophical Magazine Letters*, *61*(3), 139–146. https://doi.org/10.1080/09500839008206493

Tamblyn, I., Raty, J.-Y., & Bonev, S. A. (2008). Tetrahedral clustering in molten lithium under pressure. *Physical Review Letters*, *101*(7), 075703. https://doi.org/10.1103/PhysRevLett.101.075703

Vocadlo, L., Alfe, D., Gillan, M. J., & Price, G. D. (2003). The properties of iron under core conditions from first principles calculations. *Physics of the Earth and Planetary Interiors*, *140*(1–3), 101–125. https://doi.org/10.1016/j.pepi.2003.08.001

Vocadlo, L., de Wijs, G. A., Kresse, G., Gillan, M. J., & Price, G. D. (1997). First principles calculations on crystalline and liquid iron at Earth's core conditions. *Faraday Discussions*, *106*, 205–217. https://doi.org/10.1039/a701628j

Vosko, S. H., Wilk, L., & Nusair, M. (1980). Accurate spin-dependent electron liquid correlation energies for local spin-density calculations—A critical analysis. *Canadian Journal of Physics*, *58*(8), 1200–1211. https://doi.org/10.1139/p80-159

Waseda, Y. (1980). *The structure of non-crystalline materials: Liquids and amorphous solids*. McGraw-Hill International Book Company.

Zeng, Z.-Y., Hu, C.-E., Chen, X.-R., Cai, L.-C., & Jing, F.-Q. (2008). Magnetism and phase transitions of iron under pressure. *Journal of Physics: Condensed Matter*, *20*(42), 425217. https://doi.org/10.1088/0953-8984/20/42/425217